Meteoritics & Planetary Science 56, Nr 2, 241–259 (2021)
doi: 10.1111/maps.13615

Mineralogy, petrology, geochemistry, and chronology of the Murrili (H5) meteorite fall: The third recovered fall from the Desert Fireball Network

S. ANDERSON[1*], G. K. BENEDIX[1,2], L. V. FORMAN[1], L. DALY[1,3], R. C. GREENWOOD[4], I. A. FRANCHI[4], J. M. FRIEDRICH[5,6], R. MACKE[7], S. WIGGINS[8], D. BRITT[8,9], J. M. CADOGAN[10], M. M. M. MEIER[11,12], C. MADEN[11], H. BUSEMANN[11], K. C. WELTEN[13], M. W. CAFFEE[14,15], F. JOURDAN[1,16], C. MAYERS[1,16], T. KENNEDY[1,16], B. GODEL[17], L. ESTEBAN[17], K. MERIGOT[18], A. W. R. BEVAN[2], P. A. BLAND[1,2], J. PAXMAN[1], M. C. TOWNER[1], M. CUPAK[1], E. K. SANSOM[1], R. HOWIE[1], H. DEVILLEPOIX[1], T. JANSEN-STURGEON[1], D. STUART[19], and D. STRANGWAY[19]

[1]School of Earth & Planetary Sciences, Curtin University, GPO Box U1987, Perth, Western Australia 6845, Australia
[2]Department of Earth and Planetary Science, Western Australia Museum, Locked Bag 49, Welshpool, Western Australia 6986, Australia
[3]School of Geographical and Earth Sciences, University of Glasgow, Glasgow G12 8QQ, UK
[4]PSSRI, Open University, Milton Keynes, MK7 6AA, UK
[5]Department of Chemistry, Fordham University, Brooklyn, New York 10458, USA
[6]Department of Earth and Planetary Sciences, American Museum of Natural History, 79th Street at Central Park West, New York, New York 10024, USA
[7]Vatican Observatory, V-00120 Vatican City State
[8]Department of Physics, University of Central Florida, 4111 Libra Dr, Orlando, Florida 32816, USA
[9]Center for Lunar and Asteroid Surface Science, 12354 Research Pkwy, Suite 214, Orlando, Florida 32826, USA
[10]School of Science, UNSW Canberra, BC2610 Canberra, Australian Capital Territory 2612, Australia
[11]ETH Zurich, Institute for Geochemistry and Petrology, Zurich 8092, Switzerland
[12]Naturmuseum St. Gallen, St. Gallen 9016, Switzerland
[13]Space Sciences Laboratory, University of California, Berkeley, California 94720, USA
[14]Department of Physics and Astronomy, Purdue University, West Lafayette, Indiana 47907, USA
[15]Department of Earth, Atmospheric and Planetary Sciences, Purdue University, West Lafayette, Indiana 47907, USA
[16]Western Australian Argon Isotope Facility, JdL Centre, Curtin University, GPO Box U1987, Perth, Western Australia 6845, Australia
[17]CSIRO Earth Science and Resource Engineering, ARRC, Kensington, Western Australia 6151, Australia
[18]John de Laeter Centre, Bldg 301, Curtin University, Bentley, Western Australia 6845, Australia
[19]23 Main Street, Port Augusta, South Australia 5700, Australia
*Corresponding author. E-mail: seamus.anderson@postgrad.curtin.edu.au

(Received 17 September 2020; Revised 01, December 2020; revision accepted 03 December 2020)

Abstract–Murrili, the third meteorite recovered by the Desert Fireball Network, is analyzed using mineralogy, oxygen isotopes, bulk chemistry, physical properties, noble gases, and cosmogenic radionuclides. The modal mineralogy, bulk chemistry, magnetic susceptibility, physical properties, and oxygen isotopes of Murrili point to it being an H5 ordinary chondrite. It is heterogeneously shocked (S2–S5), depending on the method used to determine it, although Murrili is not obviously brecciated in texture. Cosmogenic radionuclides yield a cosmic ray exposure age of 6–8 Ma, and a pre-atmospheric meteoroid size of 15–20 cm in radius. Murrili's fall and subsequent month-long embedment into the salt lake Kati Thanda significantly altered the whole rock, evident in its Mössbauer spectra, and visual inspection of cut sections. Murrili may have experienced minor, but subsequent, impacts after its formation 4475.3 ± 2.3 Ma, which left it heterogeneously shocked.

INTRODUCTION

Meteorites are an important resource for understanding the origin and evolution of our solar system and come to us for free. Pieces of this precious material shower Earth every year but falls are rarely witnessed. This means that important context is missing from the meteoritic record; that is, what is the general geologic origin of these precious rocks? The Desert Fireball Network (Bland et al. 2012; Howie et al. 2017) provides a basic framework to determine that context for these rocks, allowing their source region in the solar system to be constrained. Every meteorite that has characterized orbit provides unique information that can be used to better interpret the structure of the solar system. Murrili (pronounced moo-rree-lee) is the third meteorite recovered by the Desert Fireball Network (Bland et al. 2016), after Bunburra Rockhole (anomalous achondrite), and Mason Gully (H5) (Spurný et al. 2012; Dyl et al. 2016).

Sansom et al. (2020) reported observations of a fireball lasting 6.1 s, entering the atmosphere with a speed of ~13.7 km s^{-1} at an altitude of 85 km, before slowing to ~3 km s^{-1} at an altitude of 18 km at the end of its luminous flight phase. From these observations, they determined that the meteoroid's pre-entry orbit had a semimajor axis of 2.521 ± 0.075 AU, an eccentricity of 0.609 ± 0.012, and an inclination of $3.32 \pm 0.060°$. Orbits like this, with low inclination and near the 3:1 mean-motion resonance with Jupiter, are not uncommon for other H5 chondrites with determined orbits (Jenniskens 2013; Meier 2017).

The meteorite fell in Kati Thanda (Lake Eyre) National Park, South Australia, the land of the Arabana people, on November 27, 2015. The rock specifically fell into South Lake Eyre, in a region referred to as "Murrili" by the Arabana peoples. Kati Thanda (Lake Eyre) is one of the largest landlocked lakes (>9500 km^2) in the world. The lake rarely fills completely, but even during dry seasons, there is usually some water remaining in smaller sublakes. The surface is comprised of a thin layer of halite and gypsum salts on top of brine-saturated, fossiliferous, thick clay mud (Habeck-Fardy and Nanson 2014).

This fall site posed a serious challenge for recovery. The calculated fall site was 6 km from the nearest "shore" (Fig. 1). Initial reconnaissance from light-aircraft identified what appeared to be an impact feature in the surface of the lake close to the predicted fall site (Fig. 1 inset). Our expedition to recover the meteorite was guided by members of the Arabana people, the traditional custodians of the land. In the time between the fall and the expedition (roughly 1 month), rain had obscured the original impact site. However, searching on foot and with quad bikes, in tandem with aerial and drone surveys, led to the successful recovery of the stone from a depth of 43 cm in the lake. It was recovered on December 31, 2015, <50 m away from the predicted fall line (Sansom et al. 2020).

Here, we present details of the classification, physical attributes, chronology, and geochemistry of this meteorite.

SAMPLE ALLOCATION AND ANALYTICAL METHODS

A single, fusion-crusted, heart-shaped, stone, measuring ~13 × 7 × 6 cm, weighing 1.68 kg, was retrieved (Figs. 2 and 3). From this main mass, two small wedges and a thin slab were cut for examination and analyses (Fig. 4). The cut surfaces reveal extensive alteration, due to the interaction with the salty lake clays, despite there being no obvious broken surfaces. Samples of altered and unaltered meteorite were distributed to a consortium of international researchers. Details of the allocated materials and methods are summarized in Table 1. We examined both altered and unaltered regions using optical microscopy and computed tomography. Various laboratories analyzed wedges, chips, and powders for oxygen isotope and bulk composition, cosmogenic nuclides, porosity/density, and Mössbauer spectroscopy. Details of each method are described below.

Optical Mineralogy

We examined two thin sections of Murrili using a Nikon Eclipse LV100 POL microscope at Curtin University in both transmitted (plane and polarized) and reflected light.

Computed Tomography

Two separate labs carried out X-ray computed tomography (CT)—CSIRO (Perth, Western Australia) and the American Museum of Natural History (New York, USA).

CSIRO

The sample was scanned in 3-D by X-ray CT using a Siemens SOMATOM definition AS medical scanner installed at the Australian Resources Research Centre (ARRC, Kensington, Western Australia) allowing the rapid 3-D scanning of drill cores. The instrument was calibrated using air as well as a set of five in-house rock standards of known density which are suitable for mineral resources applications (standards have densities varying from 2.7 to 4.3°g cm^{-3}). The energy of the beam was set up to have maximal phase contrast

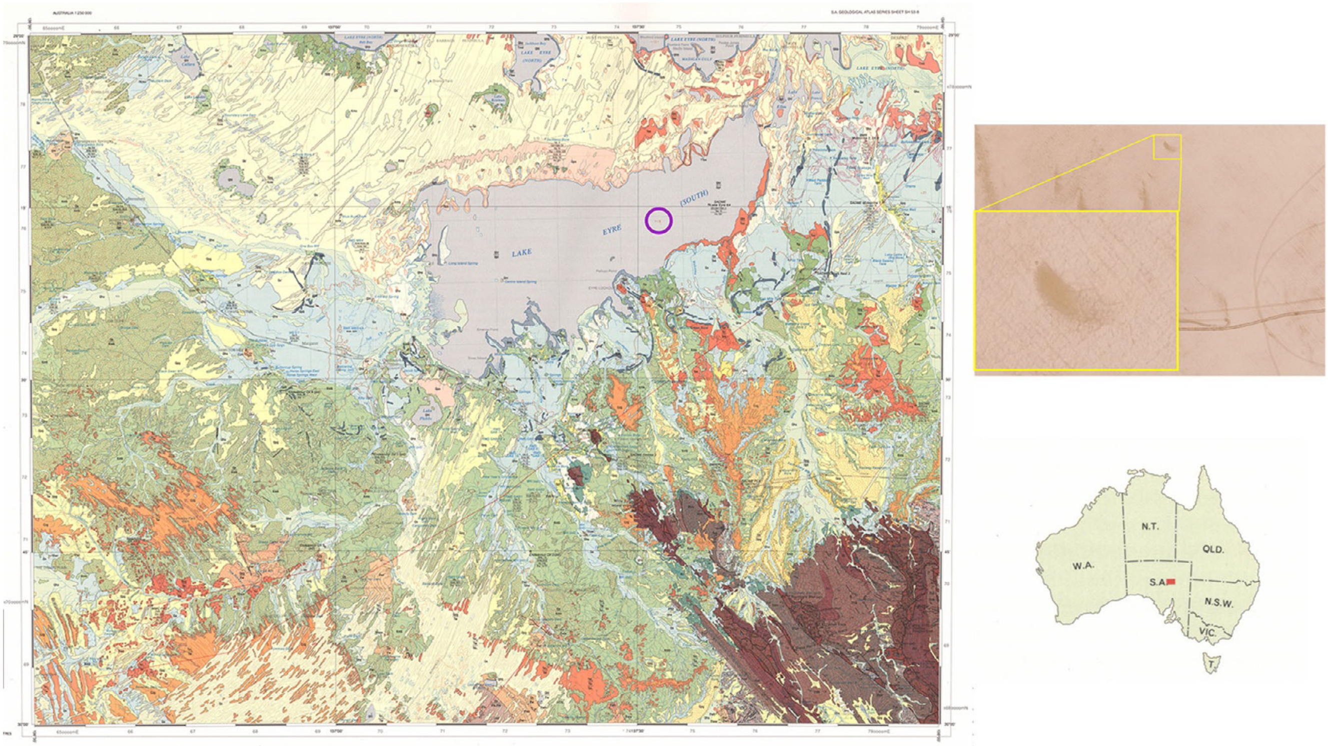

Fig. 1. Excerpted from the Curdimurka map sheet of the Kati Thanda area of South Australia (Krieg et al. 1990). Purple circle shows where Murrili was recovered. Inset shows aerial photo of the lake showing visible impact made by the meteorite. (Color figure can be viewed at wileyonlinelibrary.com.)

Fig. 2. Full mass of the Murrili meteorite, just after recovery from Lake Eyre South. (Color figure can be viewed at wileyonlinelibrary.com.)

Fig. 3. Full mass of the Murrili meteorite—ruler scale is cm. Inset shows close-up of fusion crust texture—cracks are infilled with what is most likely lake sediments. (Color figure can be viewed at wileyonlinelibrary.com.)

between the different minerals of interest (accelerating voltage of 140 kV and X-ray beam current of 1000 mA). The voxel size (a pixel in 3-D) for this overview CT scan was 220 × 220 × 100 μm. The voxel size is dictated by the size of the sample—in this case, the large meteorite meant that the overall resolution was relatively low. The XCT data were processed and analyzed using workflows developed across scale for mineral resource applications (Godel et al. 2006; Godel 2013).

Fordham/AMNH

X-ray microtomography data were collected on one of the smaller wedges (an ~50 g pyramid-shaped chunk

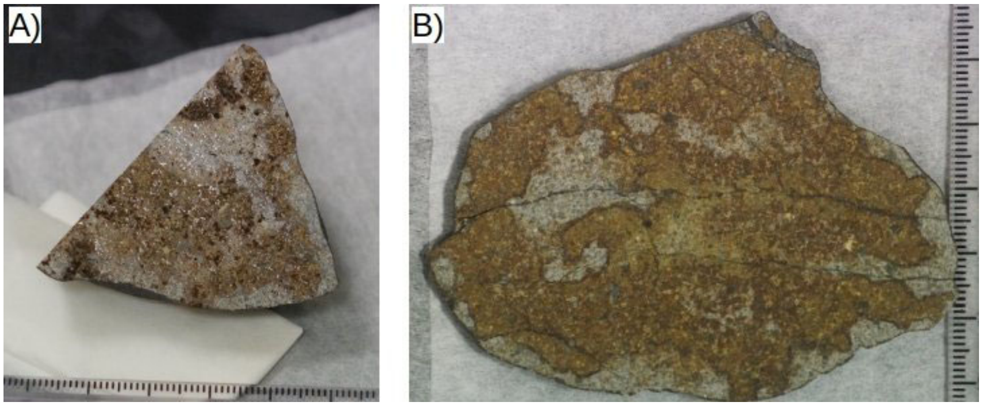

Fig. 4. Cut surfaces of Murrili. A) Wedge used for He pycnometry, magnetic susceptibility, and μCT scans. B) Slice illustrating cracks, veins, and alteration. (Color figure can be viewed at wileyonlinelibrary.com.)

of Murrili) at the American Museum of Natural History using a GE phoenix v|tome|x s240 μCT system operating with a polychromatic X-ray tube. Data were collected at several resolutions. The entire wedge was imaged at a resolution of 50.5 μm^3 per voxel edge. A subsection was imaged at a resolution of 10.0 μm^3 per voxel. The latter conditions are known to be adequate for observing morphology and size distributions of metal and sulfide grains in ordinary and other chondrites as well as examining intergranular porosity structures in partially compacted samples (Friedrich et al. 2008, 2013, 2017). From the 3-D data sets, features can be visibly identified and digitally isolated for quantitative examination, and 2-D slices (tomograms) can be extracted. Typical tomographic slices of this volume are shown in Fig. 5.

We used the method presented in Friedrich et al. (2008, 2013) to quantify the magnitude of foliation of metal grains within Murrili. Our method produces a numerical value for the strength factor, C (Woodcock 1977; Woodcock and Naylor 1983). The higher the numerical strength factor, the more pronounced the common orientation of the metal grains and the greater the foliation.

Density, Volume, Porosity, and Magnetic Susceptibility

We measured bulk volume and density on the same 50 g piece that was CT scanned by the AMNH (see above), using a NextEngine ScannerHDPro laser scanner at high resolution (Macke et al. 2015) located at UCF, with a digital scan analysis performed at the Vatican Observatory. The laser scanner produced a three-dimensional computer model of the meteorite, from which the volume enclosed by the outer surface could be calculated in the software.

Grain volume and density were determined using helium ideal gas pycnometry using a Quantachrome Ultrapyc 1200e following the procedure outlined in Macke (2010). Porosity is calculated from these two densities:

$$P = 1 - \rho_{bulk}/\rho_{grain}, \tag{1}$$

where ρ_{bulk} is the density of the whole rock, including pore spaces, while ρ_{grain} excludes pore spaces. Magnetic susceptibility was measured using an SM-30 handheld device, with volumetric and shape corrections according to Gattacceca et al. (2004) and Macke (2010).

Mineral Compositions and Modes

We determined modal mineralogy on a thick section of Murrili using a Tescan Integrated Mineral Analyzer (TIMA) housed in the Digital Mineralogy Hub (DMH) of the John de Laeter Centre at Curtin University. The automated modal analysis of the TIMA instrument was not optimized for meteorites; therefore, we generated mineral modes from element maps, using the methods outlined in Ford et al. (2008).

Mineral compositions were determined on the same thick section. Silicon, Mg, Ti, Cr, Fe, Ca, Al, and Na were measured in olivine, orthopyroxene, clinopyroxene, and chromite, with a JEOL 8530F electron microprobe based in the Centre of Microscopy, Characterization, and Analysis (CMCA) at the University of Western Australia. The probe was operated with an accelerating voltage of 20 kV and beam current of 20 nA. Well-known standards were used for calibration of the elements.

Oxygen Isotopic Analysis

Oxygen isotope analysis was carried out at the Open University using an infrared laser-assisted

Table 1. Sample allocations and methods used in this study

Method	Institution(s)	Sample type
Optical microscopy (shock analysis)	Western Australian Museum/Curtin University	Thin section
X-ray computed tomography (density and porosity)	CSIRO—Kensington/American Museum of Natural History	Whole rock/50 g wedge
Gas pycnometry (density and porosity)	Vatican Observatory/University of Central Florida (UCF)	50 g wedge (same sample used for CT)
Scanning electron microscopy/electron microprobe microanalysis (modal mineralogy and mineral composition)	Curtin University/University of Western Australia	Thick section
Laser-assisted fluorination (oxygen isotope analysis)	Open University	30–400 g chips
Inductively coupled mass spectrometry (bulk chemistry)	Fordham University	4 × 120 mg chips
Mössbauer spectroscopy (terrestrial alteration)	University of New South Wales—Canberra	300 mg powder
Noble gas analysis (cosmic ray exposure age [CRE] and meteoroid size)	Swiss Federal Institute of Technology—Zurich	100 mg chip
Cosmogenic radionuclides (CRE and meteoroid size)	University of California—Berkeley	1.1 g chip
^{40}Ar-^{39}Ar dating/^{38}Ar CRE (impact heating age/CRE)	Curtin University	2 g (fragments)

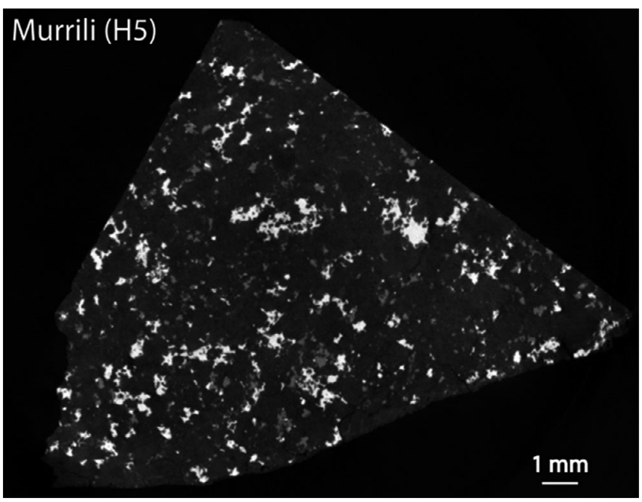

Fig. 5. Typical X-ray μCT tomogram or “slice” of the middle portion of the ~50 g wedge of Murrili collected at a resolution of 10.0 μm per voxel. The higher the grayscale intensity, the higher the density of the material. The brightest material is reduced Fe-Ni metal. The slightly darker spots are troilite. The silicates, making up the majority of the meteorite, are the medium gray material. The black area around the rock is air. Occasional round silicate shapes (chondrules), often outlined by troilite, can be distinguished in the tomogram. The area toward the bottom is a fusion-crusted surface. The straight surfaces of the rock are saw-cut surfaces.

fluorination system (Miller et al. 1999; Greenwood et al. 2017). All analyses were obtained on approximately 2 mg aliquots drawn from a larger homogenized sample powder, with a total mass of approximately 100 mg, prepared by crushing clean, interior, whole rock chips. Oxygen was released from the sample by heating in the presence of BrF_5. After fluorination, the oxygen gas released was purified by passing it through two cryogenic nitrogen traps and over a bed of heated KBr. Oxygen gas was analyzed using a MAT 253 dual inlet mass spectrometer. Overall system precision as defined by replicate analyses of our internal obsidian standard is ±0.053½ for $\delta^{17}O$; ±0.095½ for $\delta^{18}O$; ±0.018½ for $\Delta^{17}O$ (2σ) (Starkey et al. 2016).

We report oxygen isotopic analyses in standard δ notation, where $\delta^{18}O$ has been calculated as: $\delta^{18}O = ([^{18}O/^{16}O]_{sample}/[^{18}O/^{16}O]_{ref} - 1) \times 1000$ (½) and similarly for $\delta^{17}O$ using the $^{17}O/^{16}O$ ratio (where ref is VSMOW: Vienna Standard Mean Ocean Water). For comparison with the ordinary chondrite analyses of Clayton et al. (1991), $\Delta^{17}O$, which represents the deviation from the terrestrial fractionation line, has been calculated as: $\Delta^{17}O = \delta^{17}O - 0.52 \times \delta^{18}O$.

Bulk Composition

We determined bulk trace and major element compositions using inductively coupled mass spectrometry (ICPMS) at Fordham University, with methods described in Friedrich et al. (2003) and Wolf et al. (2012). We analyzed four individual chips of Murrili (126.1, 136.6, 120.5, 114.8 mg). In each aliquot, the material used for the analyses was a combination of altered and unaltered material, since the alteration was too intermingled to separate. We used a combination of concentrated HF and HNO_3 in a high-pressure microwave digestion system at 185 °C, for 15 min, to initially dissolve each chip; then, we took the resulting solution to incipient dryness on a hotplate. This was followed by treatment with concentrated $HClO_4$ and a further drying to completely dissolve the samples. The dissolved samples were taken up in 1% HNO_3 and analyzed with a ThermoElemental X-Series II ICPMS with the methods outlined in Friedrich et al. (2003) for trace elements and Wolf et al. (2012) for major and minor elements. In addition to the Murrili samples, a procedural blank and the Allende Standard Reference Meteorite were simultaneously analyzed for calibration purposes.

Mössbauer Spectroscopy

In the scope of meteorite analyses, we use Mössbauer spectroscopy to measure the oxidation states of Fe in the sample. In ordinary chondrites, Fe^0 and Fe^{2+} are of extraterrestrial origin, occurring in metallic iron, troilite, and silicates, while Fe^{3+} in iron oxides forms solely due to terrestrial contamination, for ordinary chondrites. By measuring the relative abundance of Fe^{3+} to all other iron oxidation species in the sample, we can obtain a quantitative measurement of the meteorite's weathering state (Bland et al. 1998).

The Mössbauer spectra were obtained at room temperature using a standard transmission spectrometer with a ^{57}CoRh source. The spectrometer's drive system was calibrated using a 6 μm α-Fe foil. The spectra were fitted using a nonlinear, least-squares, full Hamiltonian method.

Noble Gas Analyses

He and Ne were measured on an in-house-built sector field noble gas mass spectrometer at ETH Zurich, according to a protocol most recently described in detail by Meier et al. (2017). Two fusion-crust-free samples with masses of 45.9 and 22.6 mg, respectively, were wrapped in Al foil, loaded into the sample holder and pumped to ~10^{-10} mbar while being heated to 80 °C for 1 week to desorb atmospheric gases. For gas extraction, the samples were dropped into a crucible and heated in a single step to approximately 1700 °C by electron bombardment. Both sample analyses were bracketed by blank (empty Al foil) analyses. For analysis of all He and Ne isotopes as well as the potentially interfering species ($H_2{}^{18}O^+$, $^{12}C^{16}O_2{}^{++}$, $H^{35,37}Cl^+$), we separated He, Ne from Ar using a cryotrap cooled with liquid nitrogen. Interferences were negligible, and blank levels contributed <0.01% for He and <5% for Ne isotopes. For Ar, the blank contribution was inexplicably high (>50%), which eventually led us to discard the Ar data completely, for this approach. Noble gas concentrations and ratios were then used to determine the cosmogenic (cosmic-ray produced) ^{3}He and ^{21}Ne concentrations using multicomponent deconvolutions with radiogenic (for He only), cosmogenic, and phase Q (or air) endmembers. We used both model-based ("L&M09," Leya and Masarik 2009) and empirically determined (Dalcher et al. 2013) production rates to calculate the cosmic-ray exposure (CRE) ages from the cosmogenic concentrations. Uranium–thorium–helium radiogenic gas retention ages (^{4}He was corrected for cosmogenic contributions) were calculated based on assumed Th, U concentrations of 42 and 13 ppb, respectively, typical for H chondrites (Kallemeyn et al. 1989).

Cosmogenic Radionuclide Analysis

We used a chip of ~1.13 g for analysis of the cosmogenic radionuclides ^{10}Be (half-life = 1.36×10^6 y), ^{26}Al (7.05×10^5 y), and ^{36}Cl (3.01×10^5 y). We crushed the sample in an agate mortar and separated the magnetic (metal) from the nonmagnetic (stone) fraction. The magnetic fraction was purified by ultrasonic agitation in 0.2N HCl at room temperature, to remove attached troilite. After rinsing the metal four times with MilliQ water and once with ethanol, the separation yielded 146 mg of relatively clean metal, corresponding to 13 wt% bulk metal. The metal fraction was further purified by ultrasonic agitation in concentrated, room temperature HF for 15 min to dissolve attached silicates, yielding ~140 mg of purified metal. We dissolved ~66 mg of the purified metal in 1.5N HNO_3 along with a carrier solution containing 1.47 mg Be, 1.64 mg Al, and 4.85 mg Cl. After dissolution, we took a small aliquot (~3.6%) of the dissolved sample for chemical analysis (Mg, Fe, Co, Ni) by ICP-OES and used the remaining solution for radionuclide separation following procedures described in Welten et al. (2011). The chemical analysis of the dissolved sample yields an Mg concentration of 0.074 wt%, indicating that the purified metal contained ~0.4–0.5 wt% of silicate contamination.

After separating and purifying the Be, Al, and Cl fractions, the ^{10}Be/Be, ^{26}Al/Al, and ^{36}Cl/Cl ratios of these samples were measured by accelerator mass spectrometry (AMS) at Purdue University's PRIME Lab (Sharma et al. 2000). The measured ratios were normalized to those of well-known AMS standards (Sharma et al. 1990; Nishiizumi 2004; Nishiizumi et al. 2007) and converted to concentrations in disintegrations per minute per kg. The ^{10}Be and ^{26}Al concentrations in the metal fraction were corrected for small contributions of ^{10}Be (1%) and ^{26}Al (5.5%) from the stone fraction.

Table 2. Average olivine, orthopyroxene, and chromite mineral compositions in Murrili. Number of analyzed grains in parentheses. Fa, Fs, Wo, and chromite endmembers calculated EPMA data. Low total for chromite likely due to missing elements from analysis—most likely Mn and V, which can be up to 1 wt% each in ordinary chondrites (Bunch et al. 1967), which were not included in the EPMA analysis setup.

	Olivine (N = 15)		Orthopyroxene (N = 8)		Chromite (N = 7)	
	Average	SD	Average	SD	Average	SD
SiO_2	38.46	0.37	55.34	0.73	0.09	0.13
TiO_2	0.02	0.02	0.13	0.05	1.92	0.22
Al_2O_3	0.01	0.03	0.15	0.09	6.27	0.26
Cr_2O_3	0.02	0.03	0.13	0.06	56.95	0.75
FeO	17.77	0.44	11.10	0.15	28.92	0.25
MgO	42.92	0.36	31.21	0.28	2.85	0.13
Cao	0.03	0.03	0.59	0.15	0.04	0.04
Na_2O	0.05	0.06	0.05	0.03	0.17	0.27
Total	99.29	0.49	98.69	0.85	97.21	0.59
Fa	18.85	0.47				
Fs			16.45	0.30		
Wo			1.12	0.29		
Fe/Fe + Mg					85.07	0.57
Cr/Cr + AI					85.91	0.55

We also dissolved 106 mg of the stone fraction of Murrili, along with 2.93 mg of Be carrier and 3.68 mg of Cl carrier, in concentrated HF/HNO_3 by heating the mixture for 24 h inside a Parr Teflon digestion bomb at 125 °C. After cooling off, we separated the Cl fraction as AgCl, and removed Si as SiF_4 by repeated fuming with ~0.5 ml concentrated $HClO_4$. The residue was dissolved in diluted HCl and a small aliquot was taken for chemical analysis by ICP-OES. After adding ~5.2 mg of additional Al carrier to the remaining solution, we then separated and purified the Be and Al fractions and measured the isotopic ratios of the Be, Al, and Cl fractions by AMS. Results of the chemical analysis and AMS measurements of both the metal and stone fraction are shown in Tables 2 and 3, respectively.

^{38}Ar Age

Cosmic ray exposure (CRE) ages were also calculated based on the spallation of Ca to ^{38}Ar due to the interaction of cosmic rays with the sample. To determine the amount of ^{38}Ar in the sample per gram of Ca (Hennessy and Turner 1980), we use the cosmochron approach, which consists of an isotope correlation diagram with $^{38}Ar/^{36}Ar$ versus $^{37}Ar/^{36}Ar$ (Levine et al. 2007). The exposure age is calculated assuming a nominal production rate of ^{38}Ar from spallation of Ca of 1.81×10^{-8}cm^3 STP ^{38}Ar/g of Ca/Ma for plagioclase, 2.30×10^{-8}cm^3 STP ^{38}Ar/g of Ca/Ma for pyroxene, and a half-way value of 2.05×10^{-8}cm^3 STP ^{38}Ar/g of Ca/Ma for matrix that comprises similar quantities of comminuted plagioclase and pyroxene, best suited for the asteroid belt (Eugster and Michel 1995; Korochantseva et al. 2005). As plagioclase has very low concentrations of Fe and Ti and as the $^{38}Ar_C$ production rate from Ca is approximately 90 and 10 times that of Fe and Ti, respectively, the contribution of the latter elements to the total $^{38}Ar_c$ is negligible (Turner et al. 2013). For a full description of the approach, see Kennedy et al. (2013).

^{40}Ar-^{39}Ar Ages

To determine the Ar-Ar age of Murrili, we analyzed 2 g of material without fusion crust, which we prepared by disaggregating a larger slice to extract fragments of mineral (pyroxene and plagioclase) as well as whole chondrules. Most of our results are derived from pyroxene grains.

Samples were irradiated for 40 h and subsequently analyzed at the Western Australian Argon Isotope Facility (WAAIF) using a MAP 215-50 Mass Spectrometer equipped with a 10.4 µm CO_2 laser for stepped heating for 60 s, in accordance with Jourdan et al. (2020).

RESULTS

In this section, we present the results of each previously listed method. We start with physical properties, proceeding to chemistry, and finishing with chronology. In the discussion section, we combine these results to weave together the history of the Murrili meteorite and its subsequent fall to Earth.

Table 3. Measured concentrations of major/minor elements (wt%) and of cosmogenic radionuclides (dpm kg^{-1}) in the purified metal and nonmagnetic ("stone") fraction of the Murrili H5 chondrite fall. The Mg concentration of 0.074 wt% in the metal fraction indicates that the metal contains ~0.45 wt% of silicate contamination.

Element	Metal	Stone
	65.9 mg	106.0 mg
Mg	0.074	16.2
Al	nd	1.21
K	nd	0.12
Ca	nd	1.37
Ti	nd	0.067
Mn	nd	0.23
Fe	90.7	15.0
Co	0.48	0.011
Ni	7.9	0.64
^{10}Be	5.63 ± 0.05	21.1 ± 0.3
^{26}Al	3.99 ± 0.12	58.4 ± 1.4
^{36}Cl	24.4 ± 0.4	6.70 ± 0.11

Physical Properties

As discussed in the introduction, Murrili consists of a single stone roughly 15 cm in longest dimension. It is heart shaped with a continuous fusion crust, which shows small cracks filled with terrestrially weathered material (Figs. 3 and 4). The exterior also shows several large indentations, but there are no obvious broken surfaces.

Visual inspection of the cut surfaces of Murrili shows a heavily altered interior with a heterogeneously distributed reddish stain in the hand specimen (Fig. 4). The whole rock CT scan does not reveal obvious boundaries that would indicate brecciation, although a brecciated texture cannot be entirely ruled out (Fig. 5). Cracks are evident cutting through the fusion crust and running across whole slices. The weathering, however, is not linearly distributed away from such cracks and the alteration does not seem to affect metal uniformly, as grains both within and away from altered areas appear to be unoxidized (Fig. 4).

Alteration

Both of the ^{57}Fe Mössbauer spectra for the "unaltered" and "altered" materials in Murrili spectra are well fitted with five components. The paramagnetic doublets of olivine and pyroxene account for 70–76% of the spectral area. Troilite (FeS), Fe^{3+}, and FeNi metal comprise the remainder of the spectra. The most prominent difference between the two spectra is the relative spectral area contribution of the paramagnetic Fe^{3+} component. The "unaltered" sample has an Fe^{3+} area of slightly more than 3% whereas the "altered" sample has around 12% relative area. This dramatic increase in the relative amount of the paramagnetic Fe^{3+} component comes at the expense of the olivine, pyroxene, and metal components; the relative amount of troilite remains constant. This increase in Fe^{3+} points to an aggressive weathering process (Bland et al. 1998), in this case likely related to 30-day storage in warm, brine-saturated mud at the Lake Eyre fall site.

Another indicator of aggressive weathering may be drawn from the relative area of the silicates (olivine and pyroxene) compared to the metal. The "unaltered" spectrum has 76.1 ± 6% relative area for the silicates and 6.8 ± 4% FeNi metal, yielding a silicate to metal ratio of 11.2 ± 8. For the "altered" spectrum, these numbers are 70.0 ± 6%, 4.6 ± 4%, and 15.2 ± 14%, respectively. The olivine to pyroxene ratios are 1.59 and 1.57 for the "altered" and "unaltered" spectra, respectively, putting Murrili firmly in the H-classification according to the work of Wolf et al. (2012). However, the classification work of Verma et al. (2003) suggests that our silicon content should be accompanied by about twice as much FeNi metal than we measured, to place Murrili in the "H" region. We suggest that aggressive weathering of the FeNi component produced the paramagnetic ferric component which is possibly goethite or akaganéite.

Density and Porosity

We determined bulk density and porosity for Murrili, using both computed tomography and helium pycnometry. Coarse resolution (220 × 220 × 100 μm per voxel) CT gave a bulk volume of 467.5 cm^3 for the whole rock, which combined with the total mass of Murrili (1.68 kg), yielded a bulk density of 3.6 g cm^{-3}. Although the coarse resolution CT was not detailed enough to resolve microcracks to obtain a high-fidelity value for porosity, we were able to deduce a porosity of 3.4%. CT imaging at the highest resolution in this study (10.0 μm^3 per voxel) did not reveal any visible porosity, which suggests that the main source of Murrili's porosity is due to microcracks rather than larger vugs or intergranular porosity (Friedrich and Rivers 2013). The bulk density recorded by helium pycnometry of the 50 g wedge is 3.47 ± 0.01 g cm^{-3}, consistent with the results from the CT imaging and data extraction. Helium pycnometry also yielded a value of 3.59 ± 0.01 g cm^{-3} for grain density, which is a measure of the rock's density excluding interior void spaces. Combining bulk and grain density from helium pycnometry allowed us to determine a porosity of 3.4 ± 0.4% for Murrili.

Shock

The shock state of Murrili differs significantly between the results of the optical microscopy and fine-resolution CT. We investigated two thin sections, taken from both altered and unaltered regions, using optical microscopy. We examined 25 olivine grains in both thin sections, and found their extinction features to be straight to slightly undulatory, indicating a low, S2 shock state (Stöffler et al. 1991, 2018).

Using reflected light microscopy, we also examined the Fe,Ni metal and sulfide in the thin sections. The metallography is typical of an undisturbed, slowly cooled ordinary chondrite. In a polished mount briefly etched with a 5% Nital solution, kamacite (bcc Fe,Ni metal) shows a single set of slightly annealed and dilated Neumann bands as the only indication of mild (<130 kb), mechanical shock loading at low temperature. Many grains of taenite (fcc Fe,Ni metal) are polycrystalline, frequently comprising up to three juxtaposed taenite crystallites each delineated by tetrataenite rims and cloudy etching zones. Large grains (several hundred μm) of zoned taenite show internal decomposition to plessite (kamacite + taenite). Troilite (FeS) is generally fractured and, under crossed polarized reflected light, shows undulose, feathery, extinction. This feature is also typical of low-temperature, mechanical strain. No grains of native copper appeared in our analysis; however, grains of chromite are abundant. In terms of shock level, the metallographic features observed in the opaque phases in Murrili would equate to undulose extinction in the ferromagnesian silicates. In the polished mount examined, no indication of foliation or any other directional fabric was observed in the metallic phases.

The high-resolution CT images taken from the 50 g wedge show significant metal grain foliation. The collective orientation of metal grains observed in the 50 g wedge has a foliation strength factor of 0.75 (Fig. 6), which is consistent for a chondrite having experienced significant (S4-S5) shock-related compaction, contrary to the thin section microscopy analysis.

It is important to note that the two thin sections were taken from a separate area than the 50 g wedge. Upon further inspection of the coarse resolution CT of the whole rock, we do not see evidence of metal foliation in the thin section-sampled region, while the wedge's original area does reveal foliation. This non-uniformity in the foliation texture, along with low-shock features in the thin sections, may suggest a heterogeneous shock state across Murrili.

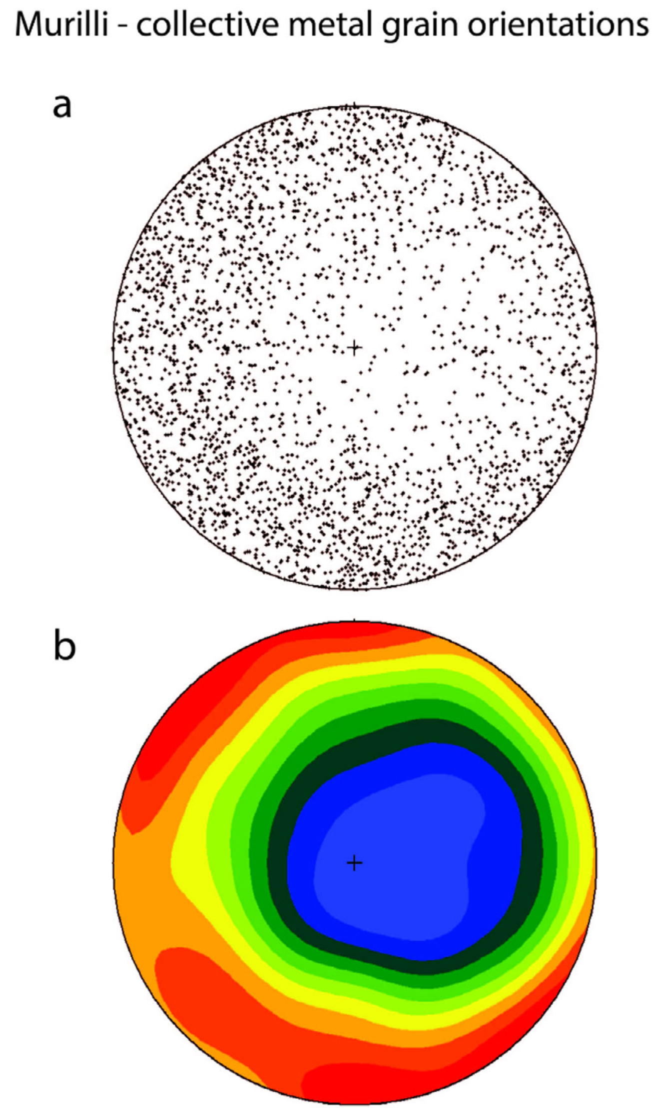

Fig. 6. a) Orientation of reduced metal grains and (b) stereogram density diagram for the Murrili H chondrite. These are lower hemisphere equal area projections. The orientation strength factor (see text) of 0.755 suggests Murrili experienced significant impact-related compaction. (Color figure can be viewed at wileyonlinelibrary.com.)

Modal Mineralogy

The mineralogy of Murrili is typical for ordinary chondrites, being dominated by olivine and pyroxene. The backscattered electron (BSE) image and elementally derived mineral maps of Murrili's thick section are shown in Fig. 7. The modal mineralogy of Murrili is plotted in Fig. 8, shown with published values for H chondrite meteorites (McSween et al. 1991; Dunn et al. 2010), for comparison. Relative to other H chondrites, there is a slight increase in orthopyroxene relative to olivine, which is generally associated with reduction processes. However, there is a coupled decrease in the abundance of plagioclase. This variation could be related to the distribution of Ca in the sample.

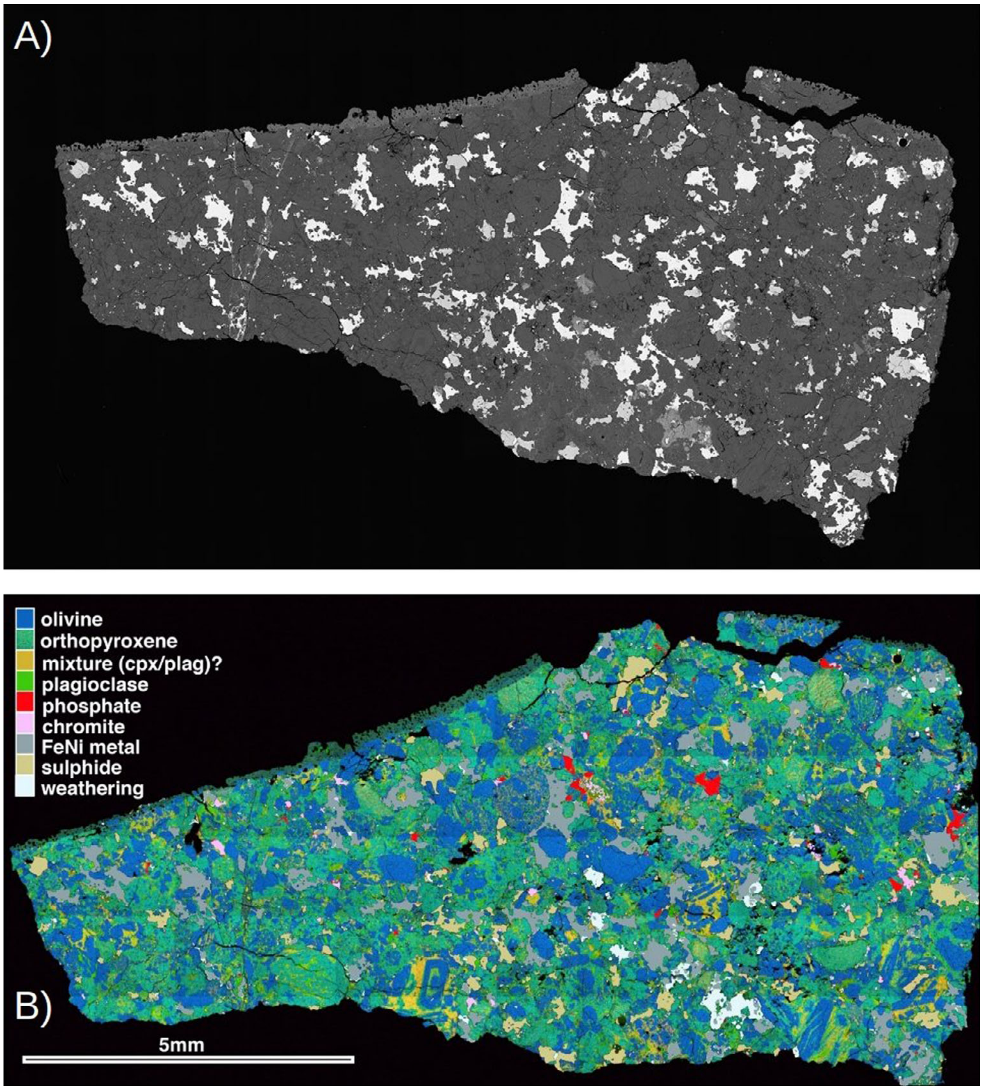

Fig. 7. Images of thin section TS1 of Murrili. A) Backscattered electron (BSE) image. B) Chemistry map created by combining maps for seven elements—Ca, Si, Mg, Fe, Ni, S, and Cr. This map distinguishes nine distinct chemistries that are tied to the mineralogies listed in the legend. CPX/Plag mix is a very fine-grained mixture of these two phases and is not distinguished at the resolution of the map. Scale bar is the same for both images. (Color figure can be viewed at wileyonlinelibrary.com.)

Composition

Mineral Compositions

Average elemental compositions of olivine, orthopyroxene, and chromite obtained using electron probe microanalysis (EPMA) are shown in Table 2. Analysis of 15 olivine grains results in an average fayalite value of 18.8 ± 0.5, indicating a significant amount of equilibration has occurred (consistent with the textural features of the sample). Orthopyroxene ($N = 7$) has an average Fs value of 16.3 ± 0.3 and an average Wo value of 1.1 ± 0.3. Additionally, Fig. 9 plots the abundance of fayalite against ferrosilite in Murrili Fe-Mg silicates, which suggests that, chemically speaking, Murrili is an H chondrite.

Bulk Chemistry

We collected data on 53 major, minor, and trace elements (Fig. 10). Typically, errors are <12% RSD. Lithophiles (Zr-Ba, $n = 29$) have a mean CI and Mg normalized abundance of 0.84 ± 0.08 (1σ). Kallemeyn et al. (1989) demonstrated that ordinary chondrites possess a mean CI and Mg normalized abundance of 0.9, indicating that Murrili is an ordinary chondrite. Within the ordinary chondrites, total siderophile element content increases in the order: LL→L→H. Siderophile elements in Murrili (Re-Pd, $n = 9$; Fig. 10) have a mean CI and Mg normalized abundance of 1.30 ± 0.15 (1σ), within errors of the H chondrite range of values.

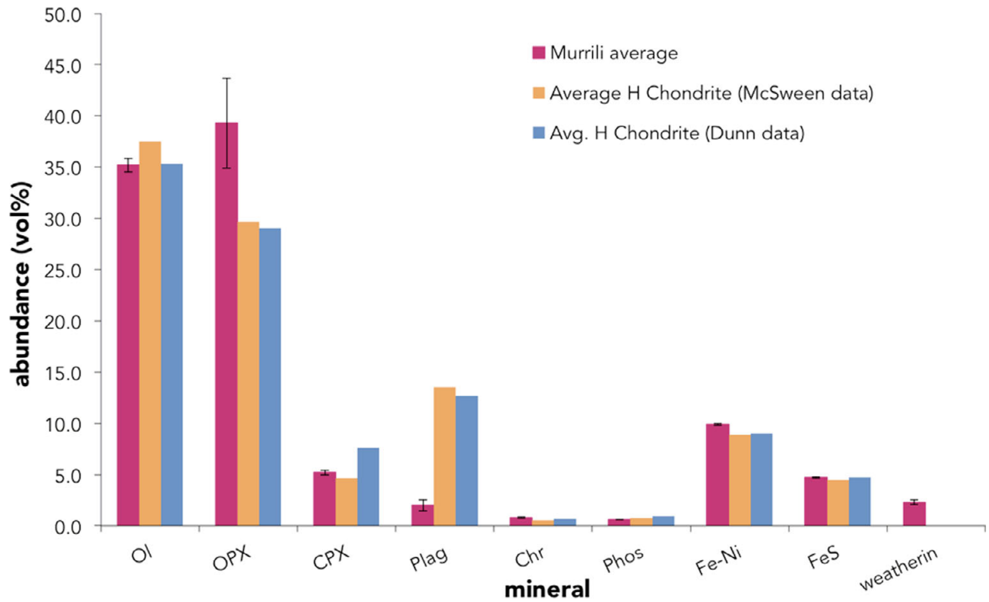

Fig. 8. Murrili's modal mineralogy based on TIMA and point counting, compared to average H chondrite values. (Color figure can be viewed at wileyonlinelibrary.com.)

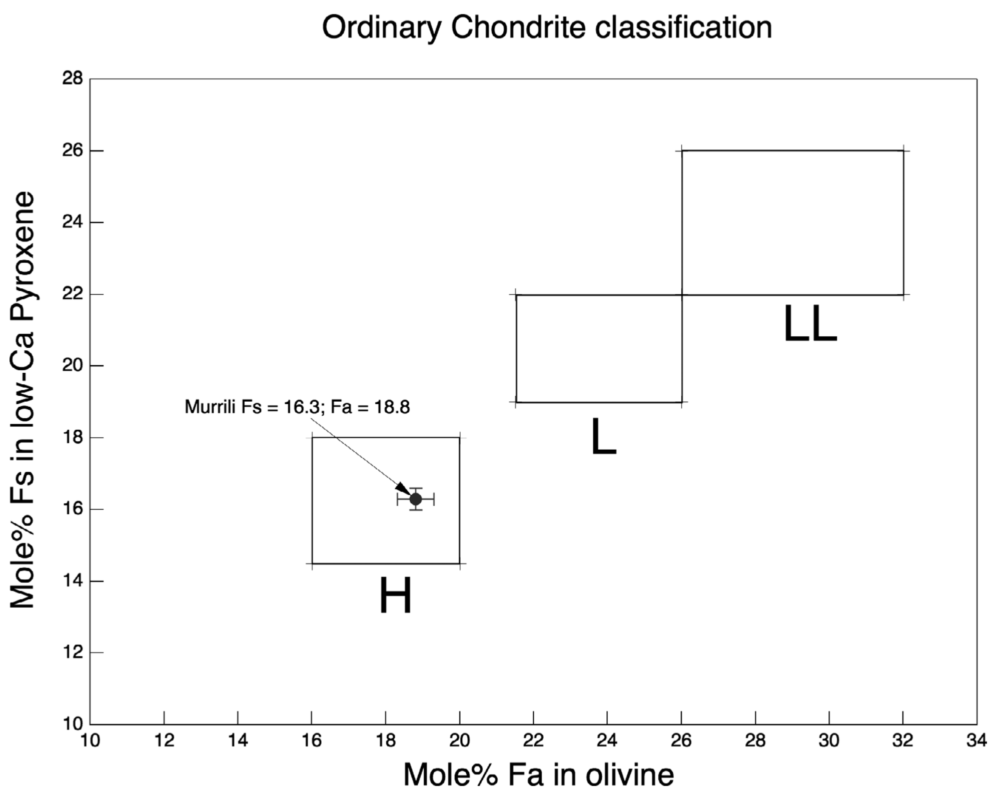

Fig. 9. Ferrosilite (Fs) value of orthopyroxene versus fayalite (Fa) value of olivine for Murrili.

It is likely that the slight enrichment in calcium, barium, and sodium relative to other lithophiles is related to terrestrial contamination, due to the month spent buried in Kati Thanda.

Oxygen Isotope Composition

The compositional classification of Murrili as H ordinary chondrite is further supported by its

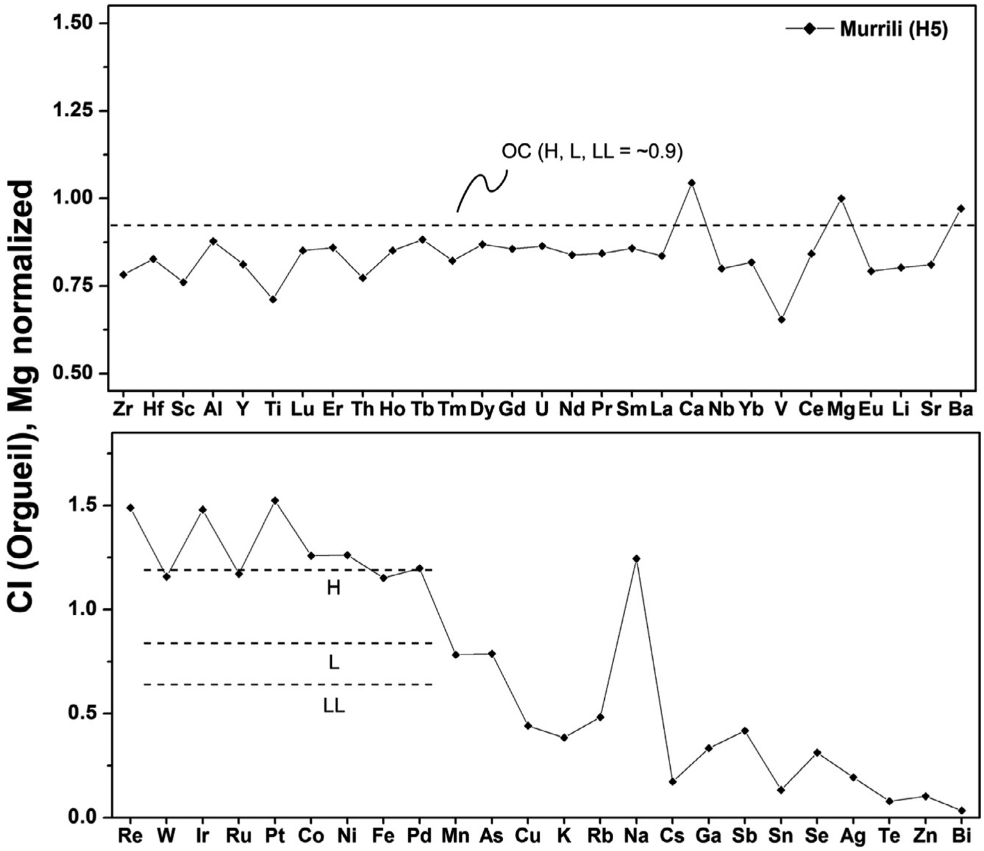

Fig. 10. CI and Mg normalized elemental abundances in the Murrili H5 chondrite.

oxygen isotopic composition. We analyzed a minimally altered piece of Murrili ($\delta^{17}O = 2.764 \pm 0.016$½; $\delta^{18}O = 3.988 \pm 0.056$½; and $\delta^{17}O = 0.691 \pm 0.013$½) as well as an altered region ($\delta^{17}O = 2.848 \pm 0.016$½; $\delta^{18}O = 4.182 \pm 0.039$½; and $\delta^{17}O = 0.673 \pm 0.004$½; errors 1$\sigma$), shown in Fig. 11. Both isotope analyses indicate consistent H chondrite classification for Murrili, falling well within the restricted range for H chondrites defined by McDermott et al. (2016; $\delta^{18}O = 4.16 \pm 0.42$½; $\delta^{17}O = 0.73 \pm 0.08$½; $n = 20$). There is a slight shift to a lower $\delta^{17}O$ value and a higher $\delta^{18}O$ value in the altered piece compared to the unaltered piece. It is, however, important to note that in terms of its oxygen isotope composition, the degree of alteration is very limited when taking into account the 2σ errors on the respective analyses.

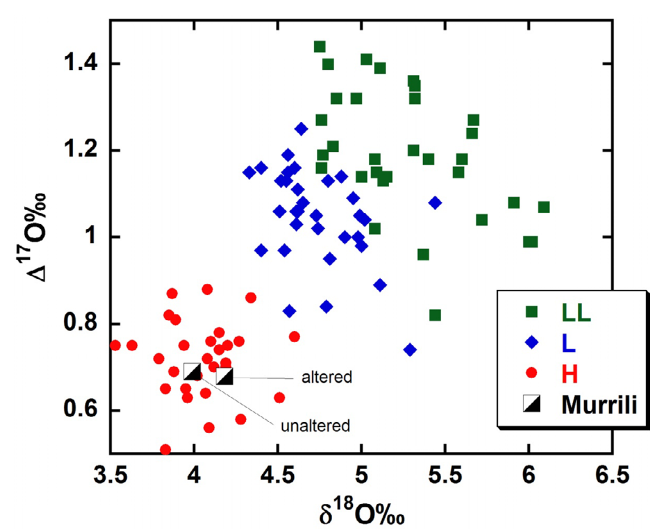

Fig. 11. Oxygen isotopic composition (Δ17O versus $\delta^{18}O$) of Murrili (both altered and unaltered) relative to the ordinary chondrite groups (from Clayton et al. 1991). $\Delta^{17}O$ is a measure of the relative difference from the terrestrial fractionation line (TFL), which is defined to be 1. Positive numbers are on parallel slope ½ lines above the TFL and negative numbers are below. Murrili plots unambiguously within the H grouping of ordinary chondrite meteorites. (Color figure can be viewed at wileyonlinelibrary.com.)

Chronology and Meteoroid Size

He and Ne Components

The Ne isotopic composition is almost identical with the cosmogenic endmember (i.e., nearly all ^{21}Ne is cosmogenic; see Table 4). A minor trapped component,

Table 4. Noble gas concentrations and derived values. All concentrations are given in units of 10^{-8} cm^3 STP per g. Given uncertainties include sample mass uncertainties. The last column gives the inverse-variance weighted average of the two samples.

Sample	Murrili NG-1	Murrili NG-2	Adopted value
Mass (mg)	45.9	22.6	—
Noble gas concentrations			
^{3}He	11.3 ± 0.4	12.6 ± 0.8	11.5 ± 0.3
^{4}He	976 ± 32	1420 ± 94	1020 ± 30
^{20}Ne	1.91 ± 0.06	2.39 ± 0.16	1.98 ± 0.06
^{21}Ne	2.01 ± 0.07	2.54 ± 0.17	2.08 ± 0.06
^{22}Ne	2.22 ± 0.07	2.80 ± 0.19	2.29 ± 0.07
Derived values			
$^{21}Ne_{cos}$	2.00 ± 0.12	2.53 ± 0.21	2.07 ± 0.17
$^{3}He_{cos}/^{21}Ne_{cos}$	5.62 ± 0.01	4.97 ± 0.01	5.18 ± 0.01
$^{22}Ne_{cos}/^{21}Ne_{cos}$	1.105 ± 0.002	1.103 ± 0.003	1.104 ± 0.002
$^{4}He_{rad}$	917 ± 42	1360 ± 130	961 ± 40

theoretically allowed within uncertainties and contributing no more than approximately 2% of the total Ne, might be of Earth atmospheric (air) or phase Q origin—the calculated concentration of cosmogenic ^{21}Ne does not depend on the choice of the trapped endmember. Similarly, the He isotopic composition of Murrili is best explained by a simple combination of cosmogenic He (all ^{3}He, and a fraction of the ^{4}He, determined by $^{4}He_{cos}/^{3}He_{cos}$ = ~6) and radiogenic He (the remaining ^{4}He after subtraction of $^{4}He_{cos}$). While some atmospheric He might theoretically be present too, it would likely be accompanied by a corresponding amount of atmospheric Ne, which already has to be very minor as found above. In combination, air He (with $^{4}He/^{20}Ne$ = ~0.3) cannot contribute more than 0.003% of the measured total He.

Meteoroid Size

Using the cosmogenic noble gas and radionuclide results, we are able to estimate the pre-atmospheric size of the meteoroid that delivered Murrili to Earth. We assume that the radionuclides are saturated, that is, the meteorite was exposed as a small object in space for >5 Ma. The $^{36}Cl/^{10}Be$ ratio of 4.33 ± 0.18 in the metal fraction is in good agreement with the $^{36}Cl/^{10}Be$-^{10}Be correlation that was obtained from a large set of meteorites with long exposure ages (Lavielle et al. 1999). The $^{26}Al/^{10}Be$ ratio of 0.71 ± 0.02 in the metal fraction also matches the average saturation ratio of 0.71 ± 0.05 that was found in a large set of meteorites. We thus conclude that the ^{36}Cl, ^{26}Al, and ^{10}Be concentrations in Murrili were all produced by a single CRE stage >5 (as independently confirmed by cosmogenic noble gases, see below).

The measured ^{10}Be and ^{26}Al concentrations in the stone and metal fraction of Murilli (Table 3) and the stone/metal ratio of 87/13 yield bulk ^{10}Be and ^{26}Al concentrations in Murrili of 19.1 ± 0.3 and 51.4 ± 1.2 dpm kg^{-1}, respectively. These values are consistent with production rates in a relatively small object with a radius $R = 10$–20 cm (Fig. 12). The concentration of cosmogenic ^{10}Be (5.6 dpm kg^{-1}) in the metal sample of Murilli is ~15% higher than the maximum calculated ^{10}Be production rates in the center of an object of 10 cm radius (L&M09). This suggests that the calculated ^{10}Be production rates in the metal fraction are too low. This is not implausible, since the uncertainty in the absolute production rates is estimated at 10–15% in the model calculations of L&M09. We increased the ^{10}Be production rates of L&M09 in the metal phase—somewhat arbitrarily—by 15% to obtain better agreement with measured ^{10}Be concentrations of up to ~6.5 dpm kg^{-1} in the metal fraction of small chondrites. The measured ^{10}Be concentrations in the stone and metal phase yield a radius of 15–20 cm for Murrili and a relatively shallow shielding depth of 3–4 cm (Fig. 13). This depth is somewhat lower than the one of >20 cm derived from the $^{22}Ne/^{21}Ne$ ratio, but the inferred size overlaps (see below).

Finally, the measured ^{36}Cl concentration of 6.7 dpm kg^{-1} in the stone fraction is consistent with calculated ^{36}Cl production rates in objects of 20–65 cm in radius (Fig. 13). However, these calculated production rates only include spallation reactions on K, Ca, Ti, Fe, and Ni, while objects larger than ~30 cm in radius also have a significant contribution of ^{36}Cl from neutron capture on Cl, which can increase the total ^{36}Cl production rates by up to a factor of 3–5 (Welten et al. 2001). Since the measured ^{36}Cl concentration in Murrili shows no evidence of neutron capture produced ^{36}Cl, this result is also consistent with a relatively small pre-atmospheric size. Based on the cosmogenic radionuclide data, we conclude that the Murrili meteorite probably

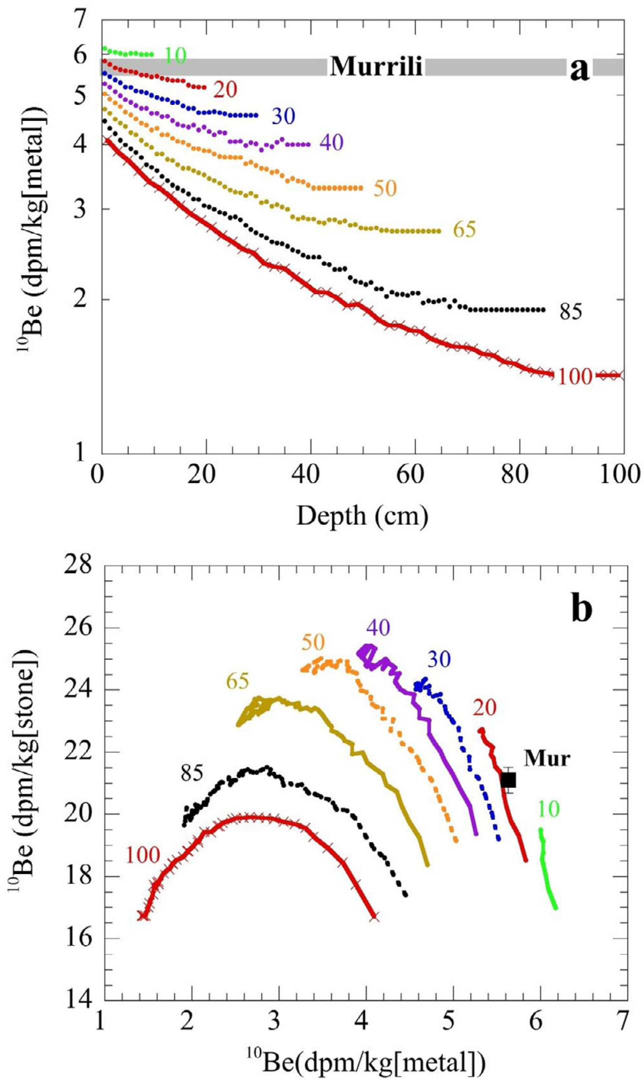

Fig. 12. Comparison of measured ^{10}Be concentrations in the metal phase (a) and in stone and metal phase (b) in Murrili with calculated production rates of ^{10}Be in metal and stone fraction of H chondrites using the model of Leya and Masarik (2009). The ^{10}Be production rates in the metal fraction were increased by 15%. (Color figure can be viewed at wileyonlinelibrary.com.)

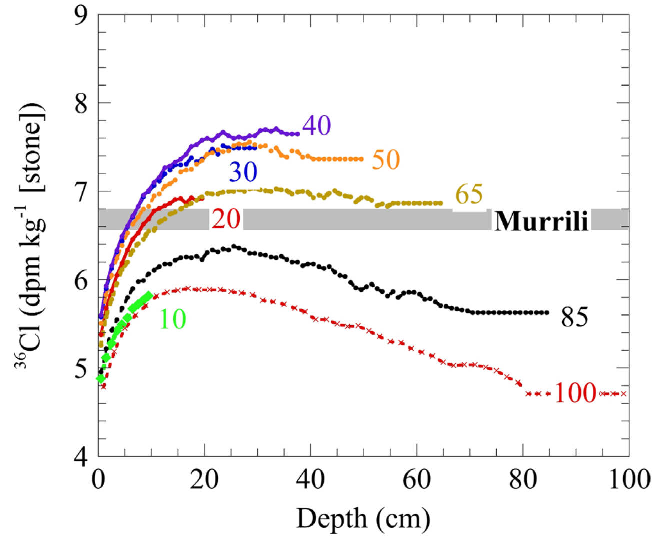

Fig. 13. Comparison of measured ^{36}Cl concentration in the stone fraction of Murrili with calculated depth profiles from the model of Leya and Masarik (2009). Production rates include spallation reactions on K, Ca, Ti, Fe, and Ni. (Color figure can be viewed at wileyonlinelibrary.com.)

came from an object with a pre-atmospheric radius of 15–20 cm.

Assuming a simple, single stage exposure, we can also use the model of L&M09 to derive the production rates of ^{3}He and ^{21}Ne for Murrili, either using the ^{22}Ne/^{21}Ne ratio as shielding parameter or the ^{26}Al concentration, which is more sensitive to shielding and shows a good correlation with the ^{21}Ne production rate in objects <50 cm in radius.

Based on the Ne isotopic composition of Murrili (^{22}Ne/^{21}Ne = 1.10), only the smallest modeled meteoroid given by L&M09 (with R = 10 cm) can be excluded, since all shielding depths have ^{22}Ne/^{21}Ne > 1.10. Since no R = 15 cm model is provided by L&M09, we technically cannot exclude the radius suggested by the radionuclide and fireball results (approximately 15 cm). The next larger meteoroid provided by L&M09, with R = 20 cm, has a compatible zone at a shielding depth of 14 ± 1 cm. For even larger modeled meteoroids, the compatible zone moves to slightly more shallow shielding depths (e.g., 10 ± 1 cm within an R = 50 cm meteoroid). The measured (average) ^{3}He/^{21}Ne ratio of 5.2 is close to the range of values expected under these shielding conditions (approximately 5.2–5.6, depending on R), providing further support for a small pre-atmospheric size and minimal to no gas loss during its transfer to Earth.

Cosmic Ray Exposure

In addition to extrapolating a pre-atmospheric entry size for the meteoroid, the cosmic ray produced ^{3}He and ^{21}Ne concentrations are used to calculate the CRE age. For the noble gas interpretation (excluding Ar), we used the inverse-variance-weighted concentrations of 11.5 (^{3}He) and 2.07 (^{21}Ne) × 10^{-8} cm^{3} STP per g. The empirically derived ^{3}He and ^{21}Ne production rates of (1.65–1.78) × 10^{-8} cm^{3} STP per (g Ma) and (3.2–3.4) × 10^{-9} cm^{3} STP per (g Ma; L&M09; Dalcher et al. 2013) yield a CRE age of 6.1–7.0 Ma. This determines the time elapsed since Murrili was separated as a small object from its parent body in the asteroid belt, and overlaps with the main CRE age peak at ~7 Ma (Marti and Graf 1995) or ~6–10 Ma (Herzog and Caffee 2014) for H chondrites.

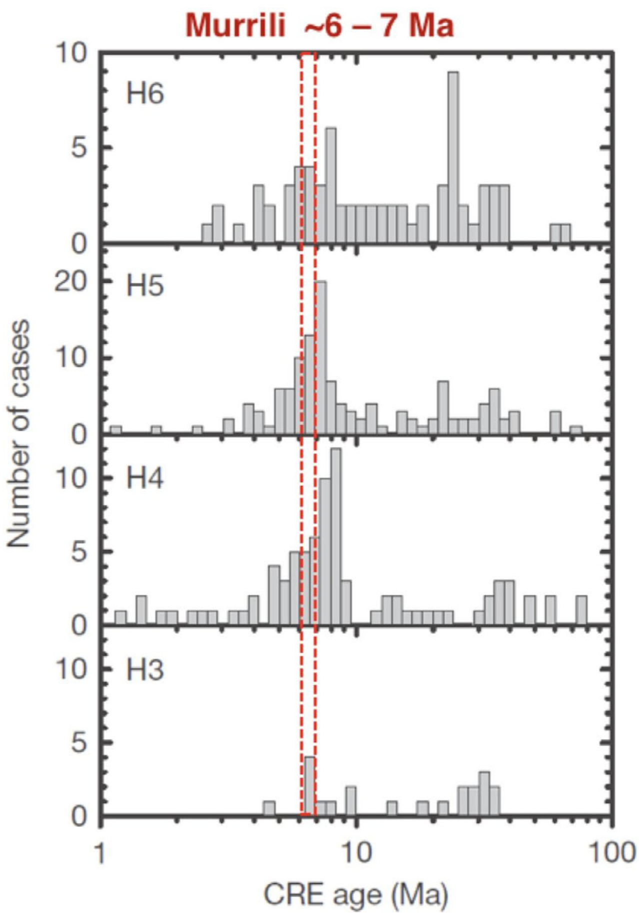

Fig. 14. Cosmic ray exposure (CRE) ages for other H chondrites. Murrili falls into the (possibly double) peak around 6–8 Ma. (Color figure can be viewed at wileyonlinelibrary.com.)

Based on the measured ^{26}Al concentration of 51.4 dpm kg^{-1} for the Murrili H chondrite, the model of L&M09 yields ^{3}He and ^{21}Ne production rates of 1.65 and 0.27×10^{-8} cc STP per g per Ma, respectively, for Murrili. This method yields CRE ages of 7.0 Ma for ^{3}He and 7.7 Ma for ^{21}Ne, which still overlap within error with the main H chondrite CRE age cluster at 6–10 Ma (Fig. 14). Radiogenic ^{4}He (corrected for a cosmogenic contribution with $^{4}He_{cos}/^{3}He_{cos} = 5.2$) yields a U,Th-He age of 2.7 ± 0.1 Ga.

Using the ^{38}Ar data, gathered from nine samples of Murrili, we calculate a weighted mean CRE age of 7.12 ± 0.41 Ma. The relative agreement of values obtained from ^{3}He, ^{21}Ne, and ^{38}Ar suggests minimal noble gas loss during atmospheric entry, or during its terrestrial exposure.

^{40}Ar-^{39}Ar Age

Our ^{40}Ar-^{39}Ar dating analysis yielded three plateaus and two smaller plateaus, all concordant with an average age of 4475.3 ± 2.3 Ma. Across our 17 samples, there was little variation in age results, although two samples did yield ages up to 1 Ga younger than the rest. This suggests minor subsequent impact heating events that had different results on the Ar system, depending on the crystal size and type, along with local porosity.

DISCUSSION

Classification

The bulk olivine and pyroxene compositions of Murrili fall squarely within the H chondrite fields (Figs. 7–9). The siderophile elements are more diagnostic than the lithophile elements (Fig. 10), in line with the metal/sulfide ratio. The oxygen isotopic composition also confirms that Murrili is an H-type ordinary chondrite. Its magnetic susceptibility (log $\chi = 5.30$) too is consistent with other, weathered, H chondrites. The modal mineralogy of Murrili is broadly consistent with ordinary chondrites, being dominated by Fe-Mg silicates and containing metal and sulfide in a proportion roughly similar to that of H chondrites (McSween et al. 1991; Dunn et al. 2010). The modal mineralogy derived from the thin section supports the estimate derived from CT scan density percentages. Of the whole rock, 73% has a density consistent with silicate mineralogy—the remaining 27% comprises metal, sulfide, and minor minerals (phosphates and chromite, etc.). It is interesting to note that the modal mineralogy of the thin section shows a high abundance of orthopyroxene relative to olivine and a significant decrease in abundance of plagioclase relative to other chondrites—which may indicate a slight variation in oxidation states compared to other H chondrites, or potentially a redistribution of Ca. Mason Gully, another fall recovered by the DFN, showed this modal mineralogical anomaly as well (Dyl et al. 2016).

The lack of distinct chondrule boundaries, the absence of striated pyroxene, the lack of chondrule glass, an overall recrystallized texture, and the equilibrated silicate mineral compositions ($Fa_{18.8\pm0.5}$; $Fs_{16.4\pm0.3}$; $Wo_{1.1\pm0.3}$; Scott et al. 1986) indicate that the petrographic type of this meteorite is most consistent with type 5. The morphologies of the CT scans of both the main mass and the 50 g piece support this.

The above modal mineralogy, mineral chemistry, morphologies, and isotopic compositions indicate that Murrili is an H5 chondrite with extensive weathering. We will discuss shock features in detail below but based on a difference between features in thin section and CT scans, impact affected this rock heterogeneously and Murrili is a likely a breccia with indistinct lithic clasts.

Terrestrial Alteration

Cut surfaces reveal pervasive alteration with rusty staining heterogeneously distributed in a wormy pattern (Fig. 4). Results from Mossbauer spectroscopy (Fig. 16) point to an aggressive weathering process. Both of these results are consistent with the length of time Murrili resided in the salt lake environment, allowing alteration to occur throughout the low-porosity rock. There is no difference in mineral composition between the altered and unaltered regions, though there are discrepancies between the two regions in the Mössbauer analyses and the oxygen isotope measurements.

Physical Properties

Density and Porosity

For a fresh fall with an assumed low shock state (proposed by thin section analysis), Murrili's porosity of 3.4% is very low. The average H fall is about 10% porous while most S1s within the H falls are between about 7 and 14% porous, with porosity decreasing as shock increases (Consolmagno et al. 1998).

Shock

The thin sections we examined showed an overall low (S2) shock state apparent in undulose extinction in numerous olivine grains, while the fine resolution tomographs of the 50 g wedge show metal foliation, indicative of moderate (S4 and S5) shock loading (Friedrich et al. 2008). The coarse resolution tomographs of the whole meteorite show that metal foliation is present throughout most of the rock, including the region that the wedge was taken from, but excluding the locality where the thin sections were sampled.

Although we did not observe brecciation at the microscale in either of our thin sections or in our CT tomographs, larger cracks are apparent in the wedge we used for both helium pycnometry and fine resolution CT (Fig. 4a). Due to the heterogeneous nature of its shock features, as well as a lack of microscale brecciated texture, Murrili is most likely brecciated at the cm–dm scale.

Chronology

The ^{40}Ar-^{39}Ar age of Murrili is dated to 4475.3 ± 2.3 Ma, which fits well with other H chondrites (Trieloff et al. 2003). Although we recorded some minor variation in two samples, which may suggest post-formation impact events, we do not see apparent evidence of major brecciation. This most likely suggests minor impact events just after recrystallization. This chronological anomaly along with the heterogeneous nature of Murrili's shock state will be investigated further in a forthcoming publication.

Murrili has a CRE age that falls within the broad 6–10 Ma peak in the CRE age histogram of the H chondrites (Graf and Marti 1995). Graf and Marti (1995) suggested that this peak, which contains ~50% of the H chondrites, might be a double peak, with ages around ~6 Ma more prominent for H5 chondrites than for other petrographic types of H chondrites, which typically have CRE ages around ~8 Ma (Fig. 15). The CRE age of Murrili, which is between 6.1 and 7.7 Ma depending on the method chosen, cannot provide further support for this pattern. The relatively high ^{3}He/^{21}Ne ratio suggests that Murrili is derived from a rather small meteoroid with a radius of ~20 cm (certainly >10 cm). This is compatible with the estimated radius of ~14 cm inferred by Sansom et al. (2020) from the photographic observations of the fireball, and the estimated radius of 15–20 cm from the cosmogenic radionuclide data.

CONCLUSIONS

Murrili formed as an H5 chondrite on its parent body 4475.3 ± 2.3 Ma, experiencing subsequent but minor impacts which left it heterogeneously shocked and brecciated at the cm-scale. Approximately 6–8 Ma, Murrili's precursor meteoroid was separated from its parent body, at a size of 15–20 cm in radius. Just prior to its collision with Earth, the meteoroid had an orbit with a semimajor axis of ~2.5 AU with a low inclination, near the 3:1 mean resonance with Jupiter, which is not uncommon for other orbitally determined H5s.

The meteoroid entered the Earth's upper atmosphere at a speed of ~13 km s^{-1}, over South Australia on the night of November 27, 2015 at 9:15 pm (local time). After it stopped ablating, it eventually fell into the salt lake: Kati Thanda (South Lake Eyre), punching through the upper crust of the lake, embedding itself 42 cm below the surface. Although there was no standing water on the surface of the lake during the fall, the clay soil below the surface was saturated with a salt brine, which heavily weathered some portions of the meteorite before it was recovered a month later. The main characteristics of Murrili and how we measured them are listed in Table 5.

Although Murrili has been thoroughly characterized here, one anomaly remains unexplored with this meteorite: its shock history. Most of the ^{40}Ar-^{39}Ar measurements for Murrili indicate an age of 4475.3 ± 2.3 Ma, except for two readings that yield ages up to 1 Ga younger. This, combined with Murrili's

Table 5. Summary of the characteristics appearing in the Murrili meteorite.

Property	Results	Method
Petrologic type	H5	Optical microscopy, computed tomography, laser-assisted fluorination, TIMA, electron microprobe, magnetic susceptibility
Porosity	3.4%	Computed tomography
	3.4 ± 0.4%	Helium pycnometry
Bulk density	3.6 g cm^{-3}	Computed tomography
	3.47 ± 0.01 g cm^{-3}	Helium pycnometry
Grain density	3.59 ± 0.01 g cm^{-3}	Helium pycnometry
Magnetic susceptibility (log χ)	5.30	Magnetic susceptibility
Fe(III)/Total Fe	3–12%	Mössbauer spectroscopy
Shock classification	S2	Optical microscopy
	S4-S5	Computed tomography
^{40}Ar-^{39}Ar age	4475.3 ± 2.3 Ma	^{40}Ar-^{39}Ar dating
Cosmic ray exposure age	6.1–7 Ma	Empirical derivation
	7 Ma	L&M09 model (^{3}He)
	7.7 Ma	L&M09 model (^{3}He)
	7.12 ± 0.41 Ma	^{38}Ar concentration
Meteoroid size (radius)	15–20 cm	Noble gas concentrations
	14 cm	Kalman filter (Sansom et al. 2020)

heterogeneous shock state, requires further study into its shock history.

Acknowledgments—We thank the Arabana people, the traditional custodians of the land, for granting us permission and assisting us in recovering Murrili. We also thank our two anonymous reviewers for their inputs, which helped to improve the quality of this manuscript. This work was funded by the Australian Research Council (Grant: DP200102073).

Editorial Handling—Dr. Yves Marrocchi

REFERENCES

Bland P. A., Berry F. J., and Pillinger C. T. 1998. Rapid weathering in Holbrook: An iron-57 Mössbauer spectroscopy study. *Meteoritics & Planetary Science* 33:127–129.

Bland P. A., Spurný P., Bevan A. W. R., Howard K. T., Towner M. C., Benedix G. K., Greenwood R. C., Shrbený L., Franchi I. A., Deacon G., and Borovička J. 2012. The Australian Desert Fireball Network: A new era for planetary science. *Australian Journal of Earth Sciences* 59:177–187.

Bland P. A., Towner M. C., Sansom E. K., Devillepoix H., Howie R. M., Paxman J. P., Cupak M., Cox M. A., Jansen-Sturgeon T., and Stuart D. 2016. Fall and recovery of the Murrili meteorite, and an update on the Desert Fireball Network (abstract). 79th Annual Meeting of the Meteoritical Society.

Bunch T. E., Keil K., and Snetsinger K. G. 1967. Chromite composition in relation to chemistry and texture of ordinary chondrites. *Geochimica et Cosmochimica Acta* 31:1569–1582.

Clayton R. N., Mayeda T. K., Goswami J. N., and Olsen E. J. 1991. Oxygen isotope studies of ordinary chondrites. *Geochimica et Cosmochimica Acta* 55:2317–2337.

Consolmagno G. J., Britt D. T., and Stoll C. P. 1998. The porosities of ordinary chondrites: Models and interpretation. *Meteoritics & Planetary Science* 33:1221–1229.

Dalcher N., Caffee M. W., Nishiizumi K., Welten K. C., Vogel N., Wieler R., and Leya I. 2013. Calibration of cosmogenic noble gas production in ordinary chondrites based on ^{36}Cl-^{36}Ar ages. Part 1: Refined produced rates for cosmogenic ^{21}Ne and ^{38}Ar. *Meteoritics & Planetary Science* 48:1841–1862.

Dunn T. L., Cressey G., McSween Jr H. Y., and McCoy T. J. 2010. Analysis of ordinary chondrites using powder X-ray diffraction: 1. Modal mineral abundances. *Meteoritics & Planetary Science* 45:123–134.

Dyl K. A., Benedix G. K., Bland P. A., Friedrich J. M., Spurný P., Towner M. C., O'Keefe M. C., Howard K., Greenwood R., Macke R. J., and Britt D. T. 2016. Characterization of Mason Gully (H5): The second recovered fall from the Desert Fireball Network. *Meteoritics & Planetary Science* 51:596–613.

Eugster O. and Michel T. 1995. Common asteroid break-up events of eucrites, diogenites, and howardites and cosmic-ray production rates for noble gases in achondrites. *Geochimica et Cosmochimica Acta* 59:177–199.

Ford R. L., Benedix G. K., McCoy T. J., and Rushmer T. 2008. Partial melting of H6 ordinary chondrite Kernouvé: Constraints on the effects of reducing conditions on oxidized compositions. *Meteoritics & Planetary Science* 43:1399–1414.

Friedrich J. M. and Rivers M. L. 2013. Three-dimensional imaging of ordinary chondrite microporosity at 2.6 µm resolution. *Geochimica et Cosmochimica Acta* 116:63–70.

Friedrich J. M., Wang M. S., and Lipschutz M. E. 2003. Chemical studies of L chondrites. V: Compositional patterns for 49 trace elements in 14 L4–6 and 7 LL4-6 falls. *Geochimica et Cosmochimica Acta* 67:2467–2479.

Friedrich J. M., Macke R. J., Wignarajah D. P., Rivers M. L., Britt D. T., and Ebel D. S. 2008. Pore size distribution in an uncompacted equilibrated ordinary chondrite. *Planetary and Space Science* 56:895–900.

Friedrich J. M., Ruzicka A., Rivers M. L., Ebel D. S., Thostenson J. O., and Rudolph R. A. 2013. Metal veins in the Kernouvé (H6 S1) chondrite: Evidence for pre-or syn-metamorphic shear deformation. *Geochimica et Cosmochimica Acta* 116:71–83.

Friedrich J. M., Ruzicka A., Macke R. J., Thostenson J. O., Rudolph R. A., Rivers M. L., and Ebel D. S. 2017. Relationships among physical properties as indicators of high temperature deformation or post-shock thermal annealing in ordinary chondrites. *Geochimica et Cosmochimica Acta* 203:157–174.

Gattacceca J., Eisenlohr P., and Rochette P. 2004. Calibration of in situ magnetic susceptibility measurements. *Geophysical Journal International* 158:42–49.

Godel B. 2013. High-resolution X-ray computed tomography and its application to ore deposits: From data acquisition to quantitative three-dimensional measurements with case studies from Ni-Cu-PGE deposits. *Economic Geology* 108:2005–2019.

Godel B., Barnes S. J., and Maier W. D. 2006. 3-D distribution of sulphide minerals in the Merensky Reef (Bushveld Complex, South Africa) and the JM Reef (Stillwater Complex, USA) and their relationship to microstructures using X-ray computed tomography. *Journal of Petrology* 47:1853–1872.

Graf T. and Marti K. 1995. Collisional history of H chondrites. *Journal of Geophysical Research: Planets* 100:21247–21263.

Greenwood R. C., Burbine T. H., Miller M. F., and Franchi I. A. 2017. Melting and differentiation of early-formed asteroids: The perspective from high precision oxygen isotope studies. *Geochemistry* 77:1–43.

Habeck-Fardy A. and Nanson G. C. 2014. Environmental character and history of the Lake Eyre Basin, one seventh of the Australian continent. *Earth-Science Reviews* 132:39–66.

Hennessy J. and Turner G. 1980. ^{40}Ar—^{39}Ar ages and irradiation history of Luna 24 basalts. *Philosophical Transactions of the Royal Society of London. Series A, Mathematical and Physical Sciences* 297:27–39.

Herzog G. F. and Caffee M. W. 2014. Cosmic-ray exposure ages of meteorites. In *Meteorites and cosmochemical processes*, edited by Davis A. M. Treatise on Geochemistry, vol. 1. Amsterdam: Elsevier. pp. 419–454.

Howie R. M., Paxman J., Bland P. A., Towner M. C., Cupak M., Sansom E. K., and Devillepoix H. A. 2017. How to build a continental scale fireball camera network. *Experimental Astronomy* 43:237–266.

Jenniskens P. 2013. Recent documented meteorite falls, a review of meteorite–asteroid links. Meteoroids 2013: Proceedings of the astronomical conference held at AM University, Poznan. pp. 57–68.

Jourdan F., Kennedy T., Benedix G., Eroglu E., and Mayer C. 2020. Timing of the magmatic and upper crustal cooling of differentiated asteroid 4 Vesta. *Geochimica et Cosmochimica Acta* 273:205–225.

Kallemeyn G. W., Rubin A. E., Wang D., and Wasson J. T. 1989. Ordinary chondrites: Bulk compositions, classification, lithophile-element fractionations and composition-petrographic type relationships. *Geochimica et Cosmochimica Acta* 53:2747–2767.

Kennedy T., Jourdan F., Bevan A. W., Gee M. M., and Frew A. 2013. Impact history of the HED parent body (ies) clarified by new 40Ar/39Ar analyses of four HED meteorites and one anomalous basaltic achondrite. *Geochimica et Cosmochimica Acta* 115:162–182.

Korochantseva E. V., Trieloff M., Buikin A. I., Hopp J., and Meyer H. P. 2005. ^{40}Ar/^{39}Ar dating and cosmic-ray exposure time of desert meteorites: Dhofar 300 and Dhofar 007 eucrites and anomalous achondrite NWA 011. *Meteoritics & Planetary Science* 40:1433–1454.

Krieg G. W., Callen R. A., Gravestock D. I., and Gatehouse C. G. 1990. *Natural history of the north east deserts*. Adelaide: Royal Society of South Australia.

Lavielle B., Marti K., Jeannot J.-P., Nishiizumi K., and Caffee M. W. 1999. The ^{36}Cl-^{36}Ar-^{40}K-^{41}K records and cosmic-ray production in iron meteorites. *Earth and Planetary Science Letters* 170:93–104.

Levine J., Renne P. R., and Muller R. A. 2007. Solar and cosmogenic argon in dated lunar impact spherules. *Geochimica et Cosmochimica Acta* 71:1624–1635.

Leya I. and Masarik J. 2009. Cosmogenic nuclides in stony meteorites revisited. *Meteoritics & Planetary Science* 44:1061–1086.

Macke R. J. 2010. Survey of meteorite physical properties density, porosity and magnetic susceptibility. Doctoral thesis, University of Central Florida.

Macke R. J., Kent J. J., Kiefer W. S., and Britt D. T. 2015. 3D-laser-scanning technique applied to bulk density measurements of Apollo lunar samples (abstract #1716). 46th Lunar and Planetary Science Conference.

Marti K. and Graf T. 1995. Collisional history of H chondrites. *Journal of Geophysical Research: Planets* 100:21,247–21,263.

McDermott K. H., Greenwood R. C., Scott E. R. D., Franchi I. A., and Anand M. 2016. Oxygen isotope and petrological study of silicate inclusions in IIE iron meteorites and their relationships with H chondrites. *Geochimica et Cosmochemica Acta* 173:97–113.

McSween H. Y. Jr., Bennett M. E. III, and Jarosewich E. 1991. The mineralogy of ordinary chondrites and implications for asteroid spectrophotometry. *Icarus* 90:107–116.

Meier M. M. M. 2017. Meteoriteorbits. Info-tracking all known meteorites with photographic orbits. LPI Contribution 1164. p. 1178.

Meier M. M., Welten K. C., Riebe M. E., Caffee M. W., Gritsevich M., Maden C., and Busemann H. 2017. Park Forest (L5) and the asteroidal source of shocked L chondrites. *Meteoritics & Planetary Science* 52:1561–1576.

Miller M. F., Franchi I. A., Sexton A. S., and Pillinger C. T. 1999. High precision δ^{17}O isotope measurements of oxygen from silicates and other oxides: Method and applications. *Rapid Communications in Mass Spectrometry* 13:1211–1217.

Nishiizumi K. 2004. Preparation of ^{26}Al AMS standards. *Nuclear Instruments and Methods in Physics Research* B 223–224:388–392.

Nishiizumi K., Imamura M., Caffee M. W., Southon J. R., Finkel R. C., and McAninch J. 2007. Absolute calibration of ^{10}Be AMS standards. *Nuclear Instruments and Methods in Physics Research* B 258:403–413.

Sansom E. K., Bland P. A., Towner M. C., Devillepoix H. A. R., Cupak M., Howie R. M., Jansen-Sturgeon T., Cox M. A., Hartig B. A. D., Paxman J., Benedix G., and Forman L. V. 2020. Murrili meteorite's fall and recovery from Kati Thanda. *Meteoritics & Planetary Science* 55:2157–2168.

Scott E. R., Taylor G. J., and Keil K. 1986. Accretion, metamorphism, and brecciation of ordinary chondrites: Evidence from petrologic studies of meteorites from Roosevelt County, New Mexico. *Journal of Geophysical Research: Solid Earth* 91:E115–E123.

Sharma P., Kubik P. W., Fehn U., Gove G. E., Nishiizumi K., and Elmore D. 1990. Development of ^{36}Cl standards for AMS. *Nuclear Instruments and Methods* B 52:410–415.

Sharma P., Bourgeois M., Elmore D., Granger D., Lipschutz M. E., Ma X., Miller T., Mueller K., Rickey F., Simms P., and Vogt S. 2000. PRIME lab AMS performance, upgrades and research applications. *Nuclear Instruments and Methods in Physics Research* B 172:112–123.

Spurný P., Bland P. A., Shrbený L., Borovicka J., Ceplecha Z., Singleton A., Bevan A. W., Vaughan D., Towner M. C., McClafferty T., and Toumi R. 2012. The Bunburra Rockhole meteorite fall in SW Australia: Fireball trajectory, luminosity, dynamics, orbit, and impact position from photographic and photoelectric records. *Meteoritics & Planetary Science* 47:163–185.

Starkey N. A., Jackson C. R. M., Greenwood R. C., Parman S., Franchi I. A., Jackson M., Fitton J. G., Stuart F. M., Kurz M., and Larsen L. M. 2016. Triple oxygen isotopic composition of the high-^{3}He/^{4}He mantle. *Geochimica et Cosmochimica Acta* 176:227–238.

Stöffler D., Keil K., and Scott R. D. 1991. Shock metamorphism of ordinary chondrites. *Geochimica et Cosmochimica Acta* 55:3845–3867.

Stöffler D., Hamann C., and Metzler K. 2018. Shock metamorphism of planetary silicate rocks and sediments: Proposal for an updated classification system. *Meteoritics & Planetary Science* 53:5–49.

Trieloff M., Jessberger E. K., Herrwerth I., Hopp J., Fiéni C., Ghélis M., Bourot-Denise M., and Pellas P. 2003. Structure and thermal history of the H-chondrite parent asteroid revealed by thermochronometry. *Nature* 422:502–506.

Turner G., Crowther S. A., Burgess R., Gilmour J. D., Kelley S. P., and Wasserburg G. J. 2013. Short lived ^{36}Cl and its decay products ^{36}Ar and 36S in the early solar system. *Geochimica et Cosmochimica Acta* 123:358–367.

Welten K. C., Nishiizumi K., Masarik J., Caffee M. W., Jull A. J. T., Klandrud S. E., and Wieler R. 2001. Cosmic-ray exposure history of two Frontier Mountain H-chondrite showers from spallation and neutron-capture products. *Meteoritics & Planetary Science* 36:301–317.

Verma H. C., Jee K., and Tripathi R. P. 2003. Systematics of Mössbauer absorption areas in ordinary chondrites and applications to a newly fallen meteorite in Jodhpur, Meteoritics & Planetary Science 38:963–967

Welten K. C., Caffee M. W., Hillegonds D. J., McCoy T. J., Masarik J., and Nishiizumi K. 2011. Cosmogenic radionuclides in L5 and LL5 chondrites from Queen Alexandra Range, Antarctica: Identification of a large L/LL5 chondrite shower with a preatmospheric mass of approximately 50,000 kg. *Meteoritics & Planetary Science* 46:177–196.

Wolf S. F., Compton J. R., and Gagnon C. J. 2012. Determination of 11 major and minor elements in chondritic meteorites by inductively coupled plasma mass spectrometry. *Talanta* 100:276–281.

Woodcock N. H. 1977. Specification of fabric shapes using an eigenvalue method. *Geological Society of America Bulletin* 88:1231–1236.

Woodcock N. H. and Naylor M. 1983. Randomness testing in three-dimensional orientation data. *Journal of Structural Geology* 5:539–548.